Research Article | Vol. 29, No. 14 / 5 July 2021 / Optics Express 21369
Optics EXPRESS

All-optical coherent pulse compression for dynamic laser ranging using an acousto-optic dual comb

VINCENT BILLAULT,[1,2] VICENTE DURÁN,[3] CARLOS R. FERNÁNDEZ-POUSA,[4] VINCENT CROZATIER,[2] DANIEL DOLFI,[2] AND HUGUES GUILLET DE CHATELLUS[1,*]

[1] *Univ. Grenoble Alpes, CNRS, LIPhy, 38000 Grenoble, France*
[2] *Thales Research&Technology, 1 Avenue Augustin Fresnel, 91120 Palaiseau, France*
[3] *GROC-UJI, Institute of New Imaging Technologies, Universitat Jaume I, 12071 Castello, Spain*
[4] *Engineering Research Center (I3E), Dep. of Communications Engineering, Univ. Miguel Hernández, 03202 Elche, Spain*
[*] *hugues.guilletdechatellus@univ-grenoble-alpes.fr*

Abstract: We demonstrate a new and simple dynamic laser ranging platform based on analog all-optical coherent pulse compression of modulated optical waveforms. The technique employs a bidirectional acousto-optic frequency shifting loop, which provides a dual-comb photonic signal with an optical bandwidth in the microwave range. This architecture simply involves a CW laser, standard telecom components and low frequency electronics, both for the dual-comb generation and for the detection. As a laser ranging system, it offers a range resolution of a few millimeters, set by a dual-comb spectral bandwidth of 24 GHz, and a precision of 20 µm for an integration time of 20 ms. The system is also shown to provide dynamic measurements at scanning rates in the acoustic range, including phase-sensitive measurements and Doppler shift velocimetry. In addition, we show that the application of perfect correlation phase sequences to the transmitted waveforms allows the ambiguity range to be extended by a factor of 10 up to ~20 m. The system generates quasi-continuous waveforms with low peak power, which makes it possible to envision long-range telemetry or reflectometry requiring highly amplified signals.

1. Introduction

The development of compact and versatile systems for the all-optical generation and detection of optical waves with bandwidth in the microwave (MW) range represents an active demand from several application fields. Stepped-frequency or modulated optical waves spanning several tens of GHz are required to reach sub-cm spatial resolution in fiber or free space, for its use in both coherent [1] and incoherent [2] optical frequency-domain reflectometers, lidar systems [3,4], or optical sensors interrogators [5]. The most widespread technique, based on linear chirped waves generated by direct modulation in laser diodes [6,7] show bandwidths limited to a few GHz. Different optical techniques have been implemented to extend this bandwidth, including dispersive frequency-to-time mapping [8], spectral line-by-line pulse shaping [9], or coherent stitching of chirped waveforms [10]. Also, conventional electro-optic modulation permits the access to the full modulator's bandwidth, either sequentially [2], or in the form of some specific modulating signals, such as chirped waves [11,12], digital multicarrier signals [13], or external codes [14]. These last approaches, however, only translate to the optical domain an already available resource, the MW modulation bandwidth. For this reason, compact all-optical generation techniques requiring lower modulation bandwidths are generally preferred. In a different context, the versatility of photonic signal generation is employed in radar technology not only for the agile generation and allocation of high-bandwidth radar signals, but also to incorporate a number of key functionalities, such as mixing, filtering or sampling [15].

#430998 https://doi.org/10.1364/OE.430998
Journal © 2021 Received 12 May 2021; revised 9 Jun 2021; accepted 9 Jun 2021; published 22 Jun 2021

Optics EXPRESS

Although direct detection is employed in the vast majority of these systems, coherent receivers are gaining progressive attention due to the increase in sensitivity provided by mixing with a local oscillator (LO). In parallel, digital correlation detection by pulse compression of modulated or coded signals, both in optically coherent [13,16–19] and incoherent [20,21] regimes, represents an attractive approach in scenarios of high noise, limited range or sensitivity. In pulse compression, the relevant figure of merit to assess a probe signal is its time-bandwidth product (TBP), since this parameter determines the gain provided by matched filter detection. Digital pulse compression techniques, however, require a detection bandwidth equal to the bandwidth of the optical waveforms [16,17]. In this regard, dual-comb interferometry [22] can be viewed as an all-optical alternative for performing coherent correlation detection with low detection bandwidths.

A dual-comb scheme employs two mutually coherent optical frequency combs (OFC) with different frequency spacing. One OFC, acting as a probe, is sent toward a target and its optical properties are encoded onto the probe's spectral lines. The second OFC, working as a multi-line LO, is mixed with the optical signal reflected from the target. The multi-heterodyne interference of the two combs leads to a radio-frequency (RF) spectrum originated by the beats of pairs of optical lines. Outstandingly, this process corresponds to a very efficient frequency down-conversion, requiring a detection bandwidth orders of magnitude smaller than the optical bandwidth of the combs. In the time domain, the dual-comb technique provides the cross-correlation between the probe and the reference comb and, as a consequence, can be utilized to perform coherent pulse compression of the information-bearing wave reflected from the target in a purely analog manner. Therefore, the use of dual combs combines two advantages: the pulse compression is achieved in an analog and all-optical fashion and the detection bandwidth is considerably smaller than the optical one, owing to the multi-heterodyne detection process itself. Furthermore, the refresh rate upon which this correlation is updated, is given by the difference in repetition rates of the combs, thus allowing dynamic measurements at high speeds [23]. So far, a large variety of dual-comb architectures has been demonstrated, such as those based on mutually-locked femtosecond lasers [24–26], electro-optic frequency combs [27–29], and micro-combs [30–32], for its use in a variety of applications including high-resolution spectroscopy [33] and ranging [34,35].

In this work, we propose and demonstrate a novel scheme for bandwidth-efficient, all-optical generation and coherent pulse compression of modulated optical waveforms with MW-scale bandwidth based on a bidirectional acousto-optic frequency shifting loop (AO-FSL) [36]. Previously, the use of unidirectional AO-FSL has been recognized as a simple means to generate chirped waves [37], showing direct applications in digital coherent pulse compression ranging [16,17] and, more recently, as a stepped-frequency generator for a Ka-band radar [38]. However, it is the proposed use of a bidirectional AO-FSL as a dual comb for coherent pulse compression that makes this approach much less demanding in terms of optical and electronic hardware than state-of-the-art solutions reported so far. Our system works as a dual-comb source providing repetition rates of about 80 MHz and a spectral bandwidth exceeding 20 GHz, leading to a TBP > 300 and to a range resolution < 5 mm. These figures are comparable to standard electro-optic dual-comb lidars [39] and to coherently-stitched frequency-modulated single-comb lidars [10]. Apart from the immediate benefit in terms of reduction in cost and size, the proposed system shows a number of additional advantages: instead of conventional transform-limited pulses (used, for instance, in time-of-flight laser ranging), our system permits the generation of different temporal waveforms while preserving their bandwidth. In particular, it can generate a series of long, chirped waveforms with low peak power, thus amenable to optical amplification in scenarios requiring high average power. Also, the low repetition rate of the raw cross-correlation signal enables the cost-effective integration of additional functionalities in the optical, electrical, or digital domains, such as external modulation or noise filtering, features that will be exploited in the present investigation.

Optics EXPRESS

In a series of proof-of-concept experiments, the present approach is used, first, as a ranging system, where we demonstrate the expected resolution in the millimeter range with a precision of 20 µm for averaging time of 0.02 s. Subsequently, the capability of our system to dynamically recover the complex response of linear optical circuits is illustrated by measurements of phase modulation at acoustic frequencies and by Doppler shift velocimetry of moving targets. In a final experiment, we show how the platform can be complemented by coding techniques based on external modulation. In particular, by applying perfect correlation phase sequences to the generated dual-comb waveforms, each of the combs' repetition rates are reduced by a factor of ten while maintaining its capacity to perform the mutual cross-correlation. This leads to a tenfold increase in the TBP which allows for the extension of the initial ambiguity range (AR) of ~2 m up to ~20 m (40 m roundtrip).

The article is structured as follows. First we describe the bidirectional AO-FSL developed for dual-comb ranging based on analog coherent pulse compression, and characterize its performance. Then, we report the experimental demonstration of our system for ranging, phase detection and velocimetry, and prove the capability to extend the AR. Finally, we provide conclusions and discuss future developments of the architecture.

2. Bi-directional acousto-optic frequency shifting loop

2.1. Principle of operation and experimental setup

The architecture of AO-FSLs has been described in detail in previous works [40–44]. Briefly, a (unidirectional) FSL is a recirculating fiber loop that contains three basic elements: an acousto-optic frequency shifter (AOFS) that introduces a frequency shift f_s, an erbium doped fiber amplifier (EDFA), and a tunable bandpass filter (TBPF). When the AO-FSL is fed by a CW laser, the loop generates an OFC with a line spacing given by f_s. The frequency of the n-th line is simply given by $f_n = f_0 + nf_s$, where f_0 is the frequency of the seed laser. The role of the EDFA is to compensate for the losses in the loop, while the TBPF is employed to control the comb bandwidth and to reduce the amplified spontaneous emission (ASE) originated from the EDFA. A simple steady-state model for the comb generation, which considers the saturation of the amplifier gain medium and the ASE within the EDFA, allows optimizing the loop parameters to produce broadband OFCs [43]. Thus, it is possible to obtain flat-top spectra with a number of lines (N) ranging from hundreds to thousands with a tooth spacing close to 100 MHz [37,45]. AO-FSLs have been used for many applications in microwave photonics, including signal processing and arbitrary waveform generation [46,47].

Assuming that dispersive effects inside the loop are negligible, an AO-FSL produces an OFC characterized by a quadratic spectral phase [41,42]. More precisely, the phase of the comb line at frequency f_n is given by $\varphi_n = -\pi n^2 f_s \tau_c$, where τ_c is the travel time of the light inside the loop. Experimentally, φ_n can be controlled by modifying the loop length or by varying the frequency of the RF signal applied to the AOFS. When the product $f_s\tau_c$ is equal to an integer p (a condition termed as "integer Talbot condition"), the AO-FSL generates a train of Fourier transform (FT)-limited pulses at a repetition rate of f_s [40,41]. When the value of f_s slightly departs from the integer Talbot condition by an amount Δf_s ($f_s = p/\tau_c + \Delta f_s$), the system is equivalent to a mode-locked laser after propagation through a dispersive medium with a total group delay dispersion equal to $D = \Delta f_s \tau_c/(2\pi f_s^2)$. Assuming that $|\Delta f_s| \ll f_s$, the output signal consists of a train of periodic optical chirps, with a spectral bandwidth of Nf_s and a period $1/f_s$ [16,37,48]. The chirp rate can be controlled by changing frequency f_s, its sign being determined by that of Δf_s. The duration of the chirps is equal to $|N\tau_c\Delta f_s/f_s|$, and can be set equal to $1/f_s$. In this case, the chirped waveforms are stretched so that the resulting signal is almost continuous. Moreover, owing to a frequency-to-time mapping effect that occurs in the temporal far-field, the temporal envelope of the chirps maps the spectral envelope of the OFC generated by the FSL [37,48].

Optics EXPRESS

The proposed all-optical coherent pulse compression system is based, however, on a bidirectional FSL that generates a pair of tailorable and mutually coherent OFCs [36]. Figure 1 shows the non-reciprocal FSL employed here. The entire optical setup is implemented with polarization-maintaining fiber. A narrow-linewidth (< kHz) CW laser at 1550 nm feeds the loop in both directions of propagation (clockwise and counter-clockwise). Two variable optical attenuators (VOAs) control the input power in each way. 10-dB couplers are employed to seed the loop, as well as to extract a fraction of the counter-propagating optical fields. In the common path of the loop, we insert an optical TBPF and an EDFA, both bidirectional (i.e. operating in both ways). The frequency shifter is also bidirectional, but unlike the previous components, it has a non-reciprocal behavior. This is possible by combining two circulators with two shifters (AOFS1 and AOFS2) driven at different RF frequencies f_{s1} and f_{s2}, so the counter-propagating fields experience different frequency shifts (see Fig. 1). Due to a small path imbalance between the two fiber AO shifters, the counter-propagating paths inside the loop are slightly different, leading to two different travel times τ_{c1} and τ_{c2}. Consequently, the integer Talbot condition takes place at different frequencies for each light direction. For instance, in some of the experiments shown below, FT-limited pulses are generated when $f_{s1} = 80.740$ MHz and $f_{s2} = 80.630$ MHz and the travel times are $\tau_{c1} = 148.62$ ns and $\tau_{c2} = 148.83$ ns ($p = 12$). This supposes a difference of $\delta f = f_{s1} - f_{s2} = 110$ kHz in the repetition rate of the two pulse trains. The interference of the two combs is detected by a 1.2-GHz photodiode (PDcc). The generated photocurrent is subsequently low-pass filtered and digitized by an oscilloscope.

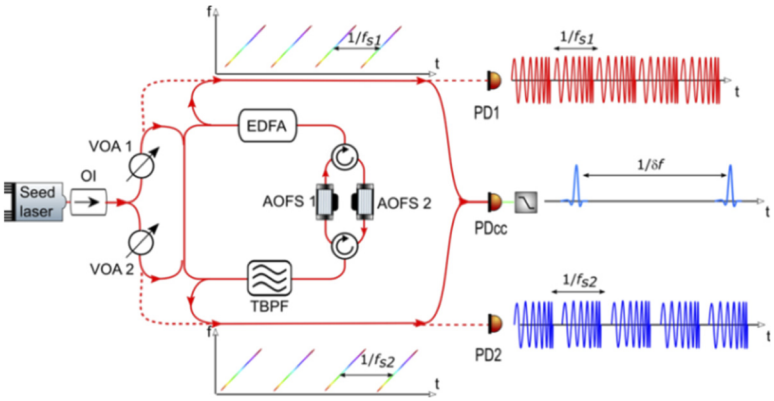

Fig. 1. Experimental setup. A bidirectional AO-FSL is seeded in both ways by a CW laser followed by an optical isolator (OI). The seed intensities are controlled by means of two variable optical attenuators (VOA 1 and VOA 2). The FSL comprises an amplifier (EDFA) and a tunable bandpass filter (TBPF), both bidirectional. A system of circulators enables to apply different frequency shifts (f_{s1} and f_{s2}) for both propagation ways. The trains of optical chirps at the output can be detected individually in the RF domain by heterodyning the optical signals with the seed laser on fast photodiodes PD1 and PD2 (dashed lines). The recombination of the optical chirps on a photodiode (PDcc) followed by a low-pass filter, generates the cross-correlation (CC) trace (rep. rate: $\delta f = f_{s1} - f_{s2}$).

An intuitive picture of the operation principle of the pulse compression procedure is given in Fig. 2. In the frequency domain, the system produces a set of two OFCs starting at f_0 and spaced respectively by f_{s1} and f_{s2}. The phases of frequency line #n in both combs are respectively equal to $-\pi n^2 f_{s1}\tau_{c1}$ and $-\pi n^2 f_{s2}\tau_{c2}$. After low pass filtering, the photodiode generates a (heterodyne) comb in the RF domain, with a frequency spacing of δf (and thus compressed by a factor $f_{s1}/\delta f$), and a spectral phase defined by $-\pi n^2(f_{s1}\tau_{c1} - f_{s2}\tau_{c2})$. When the condition $f_{s1}\tau_{c1} = f_{s2}\tau_{c2}$

Optics EXPRESS

is fulfilled, the spectral phase of the heterodyne comb is flat, and therefore the cross-correlation (CC) trace consists of a train of sharply peaked (or compressed) waveforms with a period of $1/\delta f$.

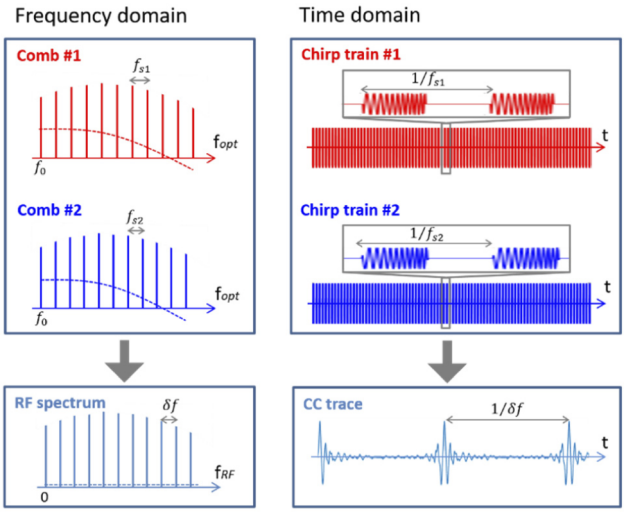

Fig. 2. Principles of pulse compression in AO dual-comb system, in the frequency (left) and in the time domain (right). Here, the vertical grey arrows represent the mixing on the photodetector followed by the low-pass filtering. In the frequency domain, contrary to conventional dual-comb systems which show a flat (or linear) spectral phase, the spectral phases of the individual combs produced in the bidirectional FSL, are quadratic (dashed curves). In the vicinity of the Talbot condition, the resulting waveforms in the temporal domain consist of chirps (see text). If $f_{s1}\tau_{c1} = f_{s2}\tau_{c2}$, the spectral phases are the same and the chirp rates of the output waveforms are identical. Then, the spectral phase of the RF spectrum resulting from the heterodyne beating of both combs is flat (or linear) and the cross-correlation trace (CC) is a periodic sequence of peaked waveforms, characteristic of pulse compression.

In the time domain, the pulse compression process can be described as follows. The electric fields emitted by the bidirectional FSL write, respectively, as [37]:

$$E_1(t) = E_0 e^{i2\pi f_0 t} \sum\nolimits_{n\geq 0} g_n e^{i2\pi n f_{s1} t} e^{-i\pi n^2 f_{s1}\tau_{c1}} + C.C. \tag{1}$$

and:

$$E_2(t) = E_0 e^{i2\pi f_0 t} \sum\nolimits_{m\geq 0} g_n e^{i2\pi m f_{s2} t} e^{-i\pi m^2 f_{s2}\tau_{c2}} + C.C. \tag{2}$$

where E_0 is the amplitude of the seed laser field, g_n are the amplitudes of the comb lines (g_n are real numbers) and $C.C.$ stands for the complex conjugate. Linear phase terms (i.e. proportional to n) have been discarded, as they only result in a global time shift. Both electric fields interfere on a photodetector and the heterodyne part of the photocurrent is given by [25]:

$$I(t) = R(t) \otimes E_1(t) E_2^*(t) + C.C. \tag{3}$$

In this equation, $R(t)$ is the low-pass filtering function and $\otimes$ stands for the convolution operation. The product of the fields, in accordance to Eqs. (1) and (2), can be expressed as:

$$E_1(t) E_2^*(t) = I_0 \sum\nolimits_{n,m\geq 0} g_n g_m e^{i2\pi[\![(nf)]\!]_{s1} - mf_{s2})t} e^{-i\pi[\![(n)]\!]^2 f_{s1}\tau_{c1} - m^2 f_{s2}\tau_{c2})} \tag{4}$$

Optics EXPRESS

where $I_0 = E_0 E_0^*$. The effect of $R(t)$ (cutoff frequency $\leq f_{s1}/2, f_{s2}/2$) is to low-pass filter all frequency components at $nf_{s1} - mf_{s2}$ where $n \neq m$. Then, the intensity rewrites as:

$$I(t) = I_0 \sum_{n\geq 0} g_n^2 e^{i2\pi n\delta f t} e^{-i\pi n^2 (f_{s1}\tau_{c1} - f_{s2}\tau_{c2})} + C.C. \tag{5}$$

If the condition $f_{s1}\tau_{c1} = f_{s2}\tau_{c2}$ is met, the resulting cross-correlation trace becomes:

$$I(t) = I_0 \sum_{n\geq 0} g_n^2 e^{i2\pi n\delta f t} + C.\,C., \tag{6}$$

which consists of a sequence of Fourier transform-limited waveforms of period $1/\delta f$. Thus, a probe waveform, say $E_1(t)$, is periodically compressed by the second, $E_2(t)$. This CC trace is a time-stretched version of the auto-correlation of the probe waveform, of period $1/f_{s1}$, and therefore the stretching ratio is equal to the bandwidth-compression factor, $f_{s1}/\delta f$. If all the N spectral lines are of the same power, $I(t)$ has the form of a periodic sine-cardinal function and the FWHM (in amplitude) of the compressed pulse in Eq. (6) is $1.21/(N\delta f)$, equivalent to $1.21/(Nf_{s1})$ in the original time scale.

2.2. Experimental characterization of the bidirectional frequency shifting loop

In our setup, the chirped waveforms generated by the bidirectional FSL can be visualized separately by heterodyning with the seed laser on fast photodiodes PD1 and PD2 (dashed lines in Fig. 1). Examples of these optical chirps, measured simultaneously for the clockwise (#2) and counterclockwise (#1) combs, are displayed in Fig. 3. The sequence of plots shows how

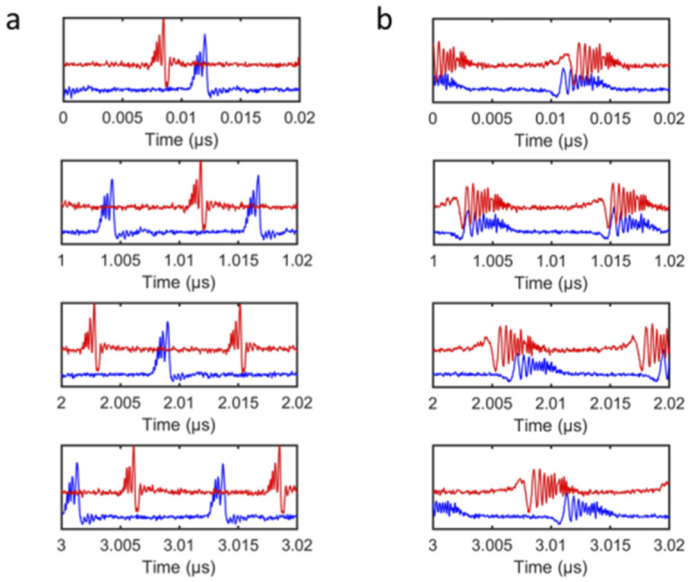

Fig. 3. Examples of chirp trains emitted by the bidirectional FSL measured at different times in two different conditions. The trains of optical chirps are measured by heterodyning with the seed laser, according to Fig. 1 (red: PD1, blue: PD2). The chirps shift over time relative to each other due to the frequency offset δf between f_{s1} and f_{s2}. a: f_{s1}=80,730 MHz and f_{s2} = 80,620 MHz. These conditions correspond to negative chirp rates (i.e. the instantaneous frequency decreases with time) [36]. b: f_{s1}=80,770 MHz and f_{s2} = 80,660 MHz, which corresponds to positive chirp rates. In a and b, the high frequency side of the chirps is filtered out by the detection bandwidth limited to 8 GHz (i.e., smaller than the comb optical bandwidth of 30 GHz).

Optics EXPRESS

the relative delay shift between the waveforms evolves with time as a result of δf. It should be noted that the bandwidth of the signals shown in Fig. 3 is limited to 8 GHz by the photodiodes. Additional output arms (not drawn in Fig. 1) allow us to record the optical spectra by means of an optical spectrum analyzer. The optical bandwidth of the two counter-propagating combs is controlled by the TBPF and can exceed 30 GHz for our setup, which corresponds to $N > 350$ lines.

Figure 4(a) shows a table with the CC traces measured for different values of f_{s1} and f_{s2}. The central plot of the table corresponds to the CC signal acquired when both combs are generated at the integer Talbot condition. The other two traces on the main diagonal are obtained from the interference of chirped waveforms that meet the condition $f_{s1}\tau_{c1} = f_{s2}\tau_{c2}$. For these FSL configurations, the detection process (matched filtering) leads to optical pulse compression in a purely analog manner. As said, this is interpreted in the spectral domain by the fact that the phases of the comb lines, labelled by n, are identical in both OFCs (see Fig. 2). Note also that the CC peaks in the main diagonal entail both positive and negative spikes. This is because the raw heterodyne signal, Eq. (6), represents the real part or in-phase component of the complex CC, and so it depends on the relative phase between the chirped waveforms generated by the two optical combs. The CC traces shown on the second row and on the second column (excluding the central plot) correspond to the configuration in which only one of the combs is set at the integer Talbot condition. The measured trace can be then understood as a down-converted version of the optical waveforms generated by the other comb. The two remaining plots of the table correspond to RF signals with an increased, positive and negative, chirp rate, due to the cross-correlation of two optical chirps with chirp rates of opposite signs.

Figure 4(b) presents an experimental trace composed of 110 interferograms, obtained when both combs are detuned from the integer Talbot condition by $\cong$ 30 kHz. As can be seen, the raw heterodyne trace consists of a series of CC peaks which, though noisy, is stable up to scales of hundreds of μs. If observed over a larger time interval, the peak's amplitudes vary slowly with time, with a typical time scale of a few seconds. This is due to the drift of the relative optical phase between the two combs, related to slow fluctuations in the non-reciprocal part of the system (i.e. the frequency shifter), where the two combs experience different paths. The raw heterodyne trace in Fig. 4(b) can be Hilbert transformed to generate its imaginary part, as shown in Fig. 4(c) with an orange trace. The correlation peak, or modulus of the analytic cross-correlation signal, can now be directly determined, as shown in Fig. 4(d). This procedure also gets rid of the influence of the phase drift. A zoom-in view of one of the correlation peaks can be observed in Fig. 4(e). The full width at half maximum (FWHM) takes a value of 34.5 ns, in good agreement with the value $1.21/(N\delta f) = 36.7$ ns deduced from Eq. (6) using $N = 300$ and $\delta f = 110$ kHz. Figure 4(f) shows the power spectrum of this CC trace. The optical bandwidth is compressed by a factor of $f_{s1}/\delta f \sim 730$. In this particular example, the RF bandwidth is set by the low-pass filter placed after the photodetector (see Fig. 1), which has a cutoff frequency of 32 MHz. The number of lines within 10 dB is then somewhat higher than 300, allowing to deduce an optical bandwidth of more than 24 GHz.

Optics EXPRESS

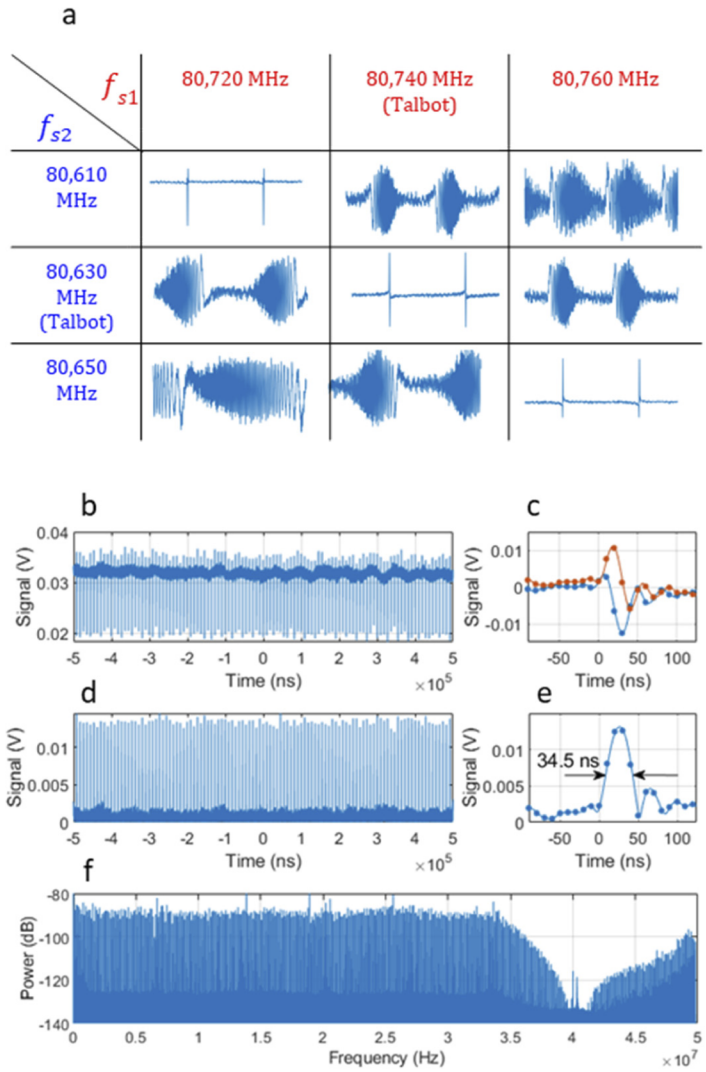

Fig. 4. Compression of the CC trace. a: CC traces measured for different values (here rounded to kHz) of f_{s1} (in red) and f_{s2} (in blue). The values $f_{s1} = 80{,}740$ MHz and $f_{s2} = 80{,}630$ MHz correspond to the so-called integer Talbot conditions, i.e. where $f_{s1}\tau_{c1}$ and $f_{s2}\tau_{c2}$ have integer values. The duration of each trace is equal to 18 µs (i.e. 2 periods at 110 kHz). b: Example of compressed CC trace (f_{s1} = 80.770 MHz, f_{s2} = 80.660 MHz). c: Performing the Hilbert transform leads to the in-phase (blue) and quadrature (orange) components of the CC peak, shown here with the dc level subtracted. d: Modulus of the analytic signal extracted from the CC trace. e: Zoom on an individual cross-correlation peak. f: RF spectrum of the CC trace measured in (a). The comb spacing is equal to $\delta f = f_{s1} - f_{s2}$=110 kHz. More than 300 lines are measured. Lines beyond 40 MHz are numerical artifacts.

3. Experimental results

3.1. Laser ranging by all-optical pulse compression

The laser ranging system based on our bidirectional AO-FSL is sketched in Fig. 5(a). At the output of one of the combs (the probe), a free-space beam is generated by means of a patch-cord

Optics EXPRESS

terminated with an FC/PC connector, followed by a fiber optic collimator. The use of a FC/PC connector produces a significant retro-reflection that provides a reference point for distance ranging. Notice that this choice hampers the measurements of absolute distances, since one should take into account the optical path inside the collimator. However, for many applications, the insertion of a PC connector is easily implementable and avoids misalignments.

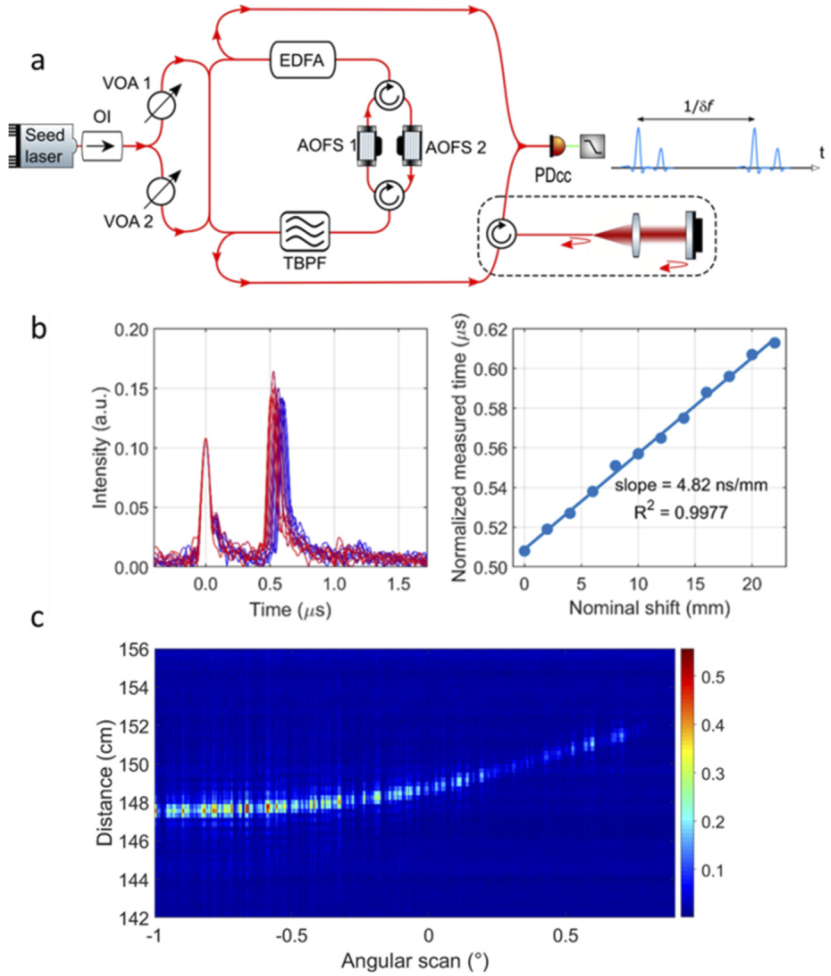

Fig. 5. Pulse compression ranging. a: Experimental set-up for ranging by pulse compression. A circulator is used to send the chirp trains #2 – the probe beam - to the target (here, a mirror mounted on a translation stage at a distance of ~10 cm from the fiber tip). A 2D scanner (not shown) can be used to sweep the probe beam on the target. A fraction of the light is reflected by the fiber tip, and is used as the origin for the distance measurement. The light back-reflected by the target is recombined with the reference chirp train (#1) on the photodiode. b: Left: CC traces recorded for different positions of the target after denoising and Hilbert transform. Right: variation of the delay with the distance of the mirror. In these measurements, f_{s1} = 80.770 MHz and f_{s2} = 80.660 MHz. c: Demonstration of profiling. The probe beam is scanned horizontally on a reflective tape wrapped around a black metal plate, located at a few meters from the fiber tip.

In a first experiment, the collimated probe beam is sent to a mirror at normal incidence. The mirror can be moved perpendicularly to the beam by a translation stage. The back-reflected light

Optics EXPRESS

is coupled into the fiber by the same collimator and, with the aid of a circulator, sent to a coupler to be mixed with the reference comb on the photodiode (PDcc). In this experiment, the values of the frequency shifts for the reference and the probe are respectively set to f_{s1} = 80.740 MHz and f_{s2} = 80.360M Hz, in order to optimize the pulse compression in the CC trace and match the condition $f_{s1}\tau_{c1} = f_{s2}\tau_{c2}$.

As in the case of the results shown in Fig. 4, the CC trace is Hilbert transformed, in order to compute the modulus of the complex CC trace. Prior to this, traces are denoised by using the fact that they are periodic (period $1/\delta f$): this enables to remove the unwanted contribution of other frequencies by applying a periodic filter with period δf to the spectrum of the CC trace [48]. The resulting modulus of the denoised, complex CC trace is composed of periodically repeated doublets, whose spacing is proportional to the relative distance between the target and the fiber tip. Figure 5(b) (left) shows a set of superimposed experimental traces, processed as in Figs. 4(c)–4(d). (Here, the traces were obtained with f_{s1} = 80.770 MHz and f_{s2} = 80.660 MHz.) Each trace corresponds to a different position of the target mirror. The first peak corresponds to the reflection on the fiber tip, and the second one to the reflection on the mirror. In Fig. 5(b) (right), we plot the variation of the delay as a function of the mirror displacement (measured on a precision translation stage). As can be seen, the spacing of the doublet varies linearly with the position of the mirror. The range resolution is set by the duration of the CC peak (i.e. 34.5 ns). Taking the bandwidth-compression factor into account, the range resolution is found to be slightly below 5 mm, which corresponds to the coherence length of the optical frequency combs (24 GHz). Our FSL system can also provide 2-D mappings by means of a scanning system (not shown in Fig. 5). It consists of a set of a rotation stage and a galvanometric mirror capable of scanning along the horizontal and vertical directions. Figure 5(c) is obtained by scanning horizontally the probe beam on a reflective tape wrapped around a black metal plate (profiling demonstration). Along that direction, the echoes from the target are produced at different depths, as can be observed in the vertical axis of the figure. The pseudo-color bar points out the relative reflectivity of each scanned point. The 2D plot is obtained by directly filling the columns of a 2D matrix with the range information derived from consecutive CC traces. The values of the axial distance have been deduced supposing free-space propagation from the tip of the fiber to the reflective tape.

Finally, we characterize the system's performance in terms of ranging precision. Here, the distance between the target and the tip of the fiber was close to 1 m roundtrip. We calculate the distance to the target by measuring the consecutive relative time delays between the reference and the measurement peaks in a 1 s-long CC trace. In this configuration, the period of an interferogram, i.e. the value of $1/f_s$, is 15.2 µs, so the experimental trace is composed of around 65800 interferograms. Then, we plot the Allan deviation of the measurements σ_{d} as a function of the integration (or averaging) time, which depends on the number of selected interferograms. The results are shown in Fig. 6.

For averaging times shorter than 20 ms, the Allan deviation decreases as the square root of the integration time, a feature characteristic of white noise processes [49]. Notice that the precision of our technique reaches 20 µm for a 20 ms-integration time. For longer averaging times, Allan deviation progressively departs from the above theoretical behavior, presumably due to the smaller number of statistical samples, and to the effect of other noise sources, such as mechanical vibrations or thermal drifts of the fibers in the measurement arm and in the non-common part of the bidirectional FSL.

3.2. Dynamic phase-sensitive measurements and Doppler shift velocimetry

The high refresh rate and the coherent nature of our ranging system allow us to measure time-varying optical phases. For the first experiment, an electro-optic phase modulator (EOPM) is inserted in the probe arm. Here, the line spacings of the two counter-propagating combs are f_{s1} = 80,770 MHz and f_{s2} = 80,660 MHz, respectively. The EOPM is driven by a sinusoidal signal

Optics EXPRESS

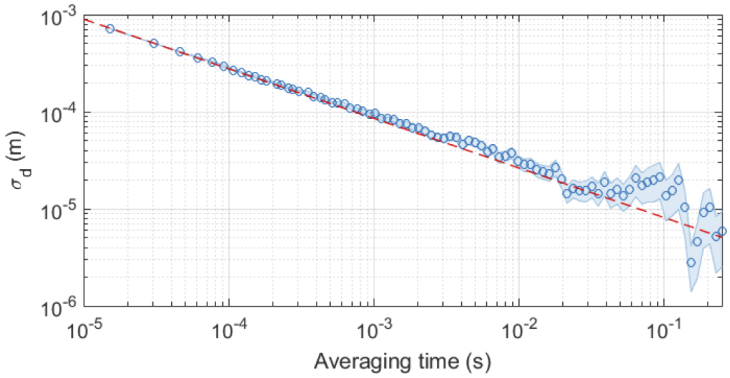

Fig. 6. Allan deviation plot. The deviation of the measurement of the distance to the target is plotted as a function of the integration time. A red dashed line with a $-1/2$ slope in the log-log plot is included to assess the evolution of the Allan deviation.

with a frequency of 3 kHz. The voltage amplitude is approximately equal to the value required to produce a phase change of π (V_π). Figure 7(a) shows an oscilloscope trace of duration 2 ms that represents the sequence of peaks describing the in-phase components of the cross-correlation between the probe and reference fields.

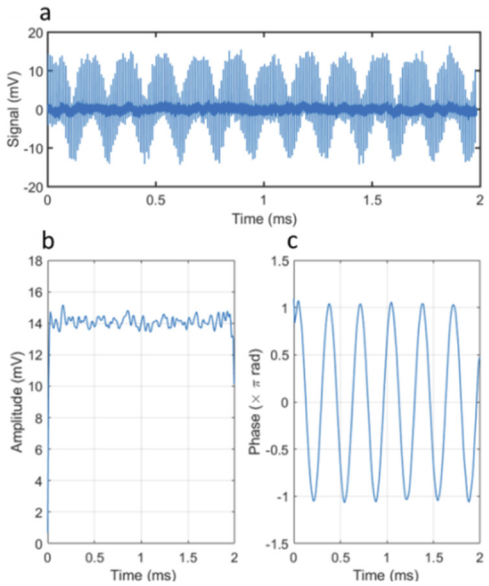

Fig. 7. Dynamic phase-sensitive measurements. a: Raw experimental CC trace obtained by inserting an EOPM in the optical path of the chirp train #2. The EOPM is driven by a sine wave at 3 kHz, while δf = 110 kHz. b, c: Reconstructed optical amplitude (b) and phase (c) in path #2.

Successive periods of the probe field undergo different propagation phases imparted by the EOPM. This phase change is slow (3 kHz) compared with the cross-correlation refresh rate ($\delta f = 110$ kHz), so the peak-to-peak variation is smooth and reflects the phase modulation induced by the EOPM. After Hilbert transform, the spectrum of the temporal trace consists of groups of spectral lines periodically repeated at δf, each group representing the spectrum of the

Optics EXPRESS

low-frequency phase modulation. The trace is then denoised by applying a periodic spectral filter with a width of 40 kHz and a period δf. Transforming back to the time domain, the complete time-varying complex cross-correlation is recovered. This quantity represents the dynamic complex modulation function, (i.e., in amplitude and phase) of the probe arm, as can be observed in Figs. 7(b) and 7(c).

Additionally, when performing laser ranging of moving targets, our interferometer is capable of measuring Doppler shifts and consequently, target speeds. The results for the Doppler velocimetry experiment are shown in Fig. 8. By means of a ranging setup similar to the one depicted in Fig. 5(a), we send the probe comb to a rotating disk that has a small area covered by a reflecting tape as shown in Fig. 8(a). The disk is oriented in such a way that the velocity of the reflecting zone has a non-zero component in the direction of the beam ($\overrightarrow{e_z}$).

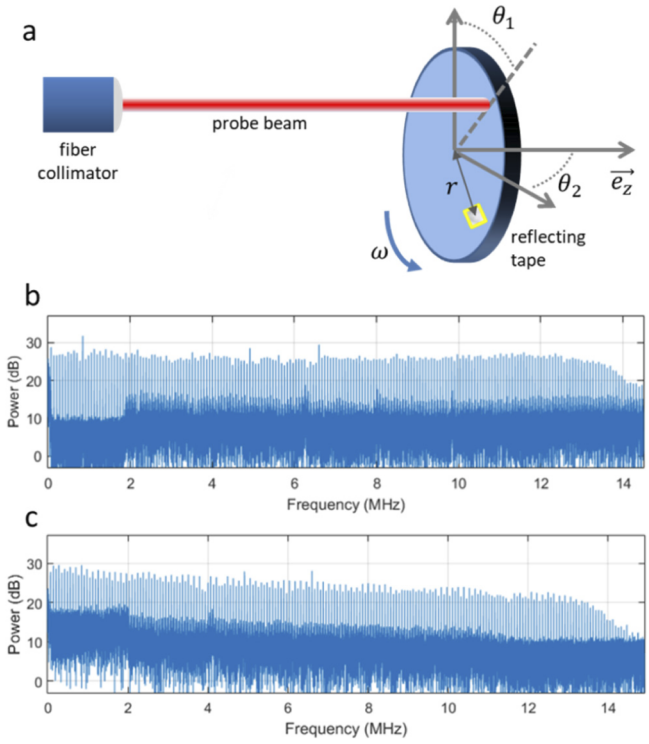

Fig. 8. Velocimetry measurements. a: Experimental set-up used for measuring the Doppler effect. The plane of the disc is tilted with respect to the direction of the probe beam by the angle θ_2. Here, due to slight experimental changes, the difference in the line spacing of both combs is now $\delta f = 70.20$ kHz ($f_{s1} = 80.702$ MHz and $f_{s2} = 80.000$ MHz). The probe chirp train (#2) is sent onto a rotating disk with a definite incidence angle. b: RF spectrum of the CC trace for a rotation speed of $N_{rps} = 3.62$ Hz. The comb of narrow lines corresponds to the beating of the reference chirp train with the chirp train reflected by the fiber tip. The frequency shifted comb results from the beating of the reference chirp train with the chirp train reflected by the rotating disk. The Doppler shift frequency calculated from Eq. (7) is 1.80 ± 0.13 MHz. c: RF spectrum of the CC trace for a rotation speed of $N_{rps} = -3.62$ Hz. The comb induced by the Doppler effect is also shifted, but reversed as compared to (b). Both RF spectra are calculated from a 20 ms acquisition trace (~ 1400 CC traces).

The number of revolutions per second, $N_{rps} = \omega/2\pi$, is controlled electrically and deduced from the measurement of the variation of the intensity of light back-reflected by the reflecting tape. The return light is collected by the fiber collimator, and combined with the reference comb

Optics EXPRESS

on the photodiode PDcc. During a rotation period, two types of interference signals can be measured. Most of the time, the light sent to the target is impinging onto a non-reflective point of the rotating disk. In that case, the retrieved RF comb is the result of the interference between the comb reflected by the PC connector (reference point, see Section B) and the reference comb. The sequence of RF lines starts then at null frequency. Eventually, the fraction of the probe beam arriving at the disk strikes the reflective tape. Then, the comb returns with a Doppler frequency shift δf_{Dopp}, which is proportional to the velocity along the laser direction (i.e. to the angular speed ω of the disk) according to:

$$\delta f_{\mathrm{Dopp}} = 2f_0 \frac{2\pi r N_{rps} cos(\theta_1)\cos(\theta_2)}{c} \tag{7}$$

where f_0 is the frequency of the seed laser, θ_1 (resp. θ_2) is the angle between the direction of the laser beam and the vertical direction (resp. the plane of the disk), see Fig. 8(a), r is the distance from the center of the disk to the reflecting tape and c is the velocity of light.

Figures 8(b) and 8(c) shows the resulting RF spectrum, composed of two interleaved combs: one is due to the reflection on the fiber tip, and the other one results from the reflection on the rotating disk. This second comb is shifted with respect to the first one by a frequency given by $\pm|\delta f_{\mathrm{Dopp}}|$, where the sign of the Doppler shift depends on the direction of rotation of the disk. A negative Doppler shift results in a reversal of the comb [Fig. 8(c)]. The broadening of the Doppler comb lines is attributed to the roughness of the reflective tape, whose reflectivity changes as it sweeps in the laser beam. Here, the Doppler shift is equal to is 1.80 ± 0.13 MHz (based on Eq. (7) with $N_{rps} = 3.62$ Hz). The uncertainty comes mainly from the measurement of the angles. As a comparison, in Figs. 8(b) and 8(c), the frequency shift is evaluated to be 1.9 MHz which is consistent with the calculated value and proves the capability of the system for Doppler shift velocimetry.

3.3. Ambiguity range expansion by the use of perfect correlation phase sequences

Similarly to conventional dual-comb ranging techniques, the ambiguity range (AR) is set by the comb line spacing. More precisely, AR $\sim c/(2f_{s1})$, where we assume that f_{s1} is the line spacing of the probe comb. The factor of 2 accounts for the round-trip between the source and the target. In our case, f_{s1} is close to 80 MHz, and the AR approaches 1.85 m. Outside this range, complementary distance measurements are required in order to find out the integer number of comb periods that separate the reflection on the target from the reference peak. This number can be also calculated by switching the roles of the probe and reference combs to make use of the Vernier effect, although at the expense of reconfiguring the comb generators and performing two sequential measurements [24]. Here, we expand the AR of the system by the application of phase sequences to the trains of chirped waveforms generated by the bidirectional FSL. In particular, we use perfect correlation Gauss sequences, characterized by the fact that their periodic autocorrelation vanishes at any non-zero time shift [50]. In this regard, it is to be noticed that this procedure is enabled by the temporal properties of the dual-comb waveforms, since they consist of trains of chirped pulses confined to their fundamental periods, $1/f_{s1}$ and $1/f_{s2}$ respectively, with negligible pulse-to-pulse overlap. By introducing the same periodic series of phase modulating signals, the periods of both combs are increased by the same factor while maintaining their capacity to perform the mutual cross-correlation leading to dual-comb pulse compression.

The modified comb-based system implemented to expand the AR is shown in Fig. 9(a). Two phase modulators (EOPM1 and EOPM2) apply the same perfect correlation phase sequence (of length q) to the chirp trains. The phase level applied to the n-th element of the sequence is set with two synchronized arbitrary waveform generators (AWGs) according to $\pi n^2/q$. In both arms, the duration of a phase level matches the period of the chirps. The periods of whole sequences

Optics EXPRESS

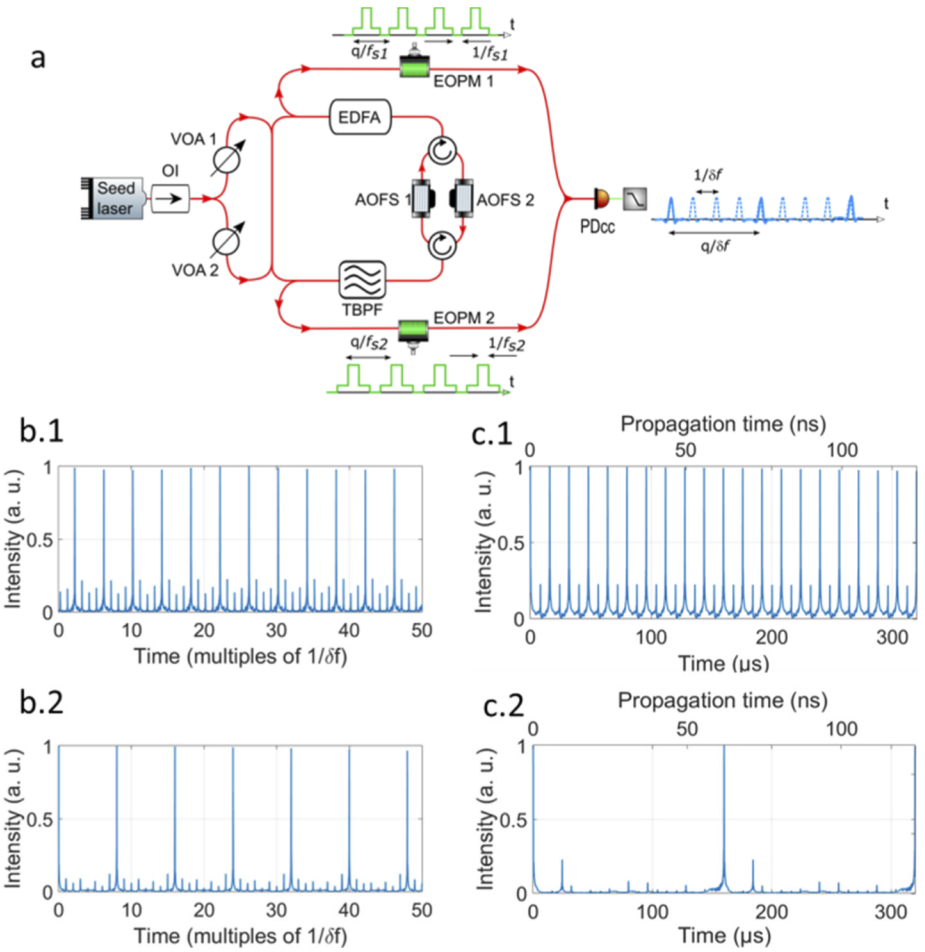

Fig. 9. Multiplication of the ambiguity range by applying perfect correlation phase sequences. a: Experimental set-up to increase the AR by the insertion of two phase modulators in the comb-based ranging system. b: Experimental autocorrelation traces after Hilbert transform and spectral filtering for $q = 4$ (b.1), and $q = 8$ (b.2). In these measurements, $f_{s1} = 80.7184$ MHz and $f_{s2} = 80.6566$ MHz (i.e. $\delta f = 61.8$ kHz). c: Evidence of AR multiplication. The distance of the target from the fiber tip is 2.83 m. c.1: No phase sequence is applied (AR: 1,85 m). c.2: A phase sequence with $q = 10$ is applied. The AR is increased to 18,5 m (see text).

are q/f_{s1} and q/f_{s2}, so a decimation by a factor of q is induced in the CC trace (i.e., constructive interference only occurs after q periods). In that way, the AR is increased by the same factor. This is illustrated in Figs. 9(b.1) and 9(b.2) that show the resulting CC traces for $q = 4$ and $q = 8$.

Each sequence is the modulus of a Hilbert transformed trace (acquired within 20 ms) after de-noising by spectral filtering. Within a single interferogram, residual peaks separated by $1/\delta f$ are visible. This is mostly due to the limited speed of the AWGs (3 ns rise time), that smoothens the phase profiles applied to the EOPMs. The expansion of the AR is evidenced in Fig. 9(c). A target is placed at an axial distance equal to 2.83 ± 0.03 m from the reference point (the fiber tip). When no phase mask is applied [Fig. 9(c.1)], the time delay between the two sets of peaks in the CC trace is equal to 8.32 μs. In the corresponding propagation time axis, taking the compression factor into account, this value would correspond to a roundtrip time from the reference point to

Optics EXPRESS

the target, equal to 6.37 ns + k×12.4 ns, where k is an integer. In other words, the relative distance of the target could be 0.96 m + k×1.85 m. To lift the ambiguity, a perfect correlation phase sequence of length $q = 10$ is applied to the chirp trains. The time delay between the two sets of peaks in the CC trace is now equal to 24.3 µs [Fig. 9(c.2)]. Following the same reasoning, this value would lead to a relative distance of the target of 2.79 m + k'×18.5 m (k' integer). Knowing that the target was placed at a relative distance smaller than 18.5 m, one can unambiguously infer a target position close to 2.79 m (i.e. $k = 1$ and $k' = 0$).

4. Conclusions

We have proposed and experimentally demonstrated a new, all-optical method for the generation and coherent pulse compression of MW-bandwidth waveforms employing low frequency elements and dual-comb cross-correlation detection. Our method is based on the generation of two trains of identical optical chirps with a slightly different repetition rate. As a timed-domain detection technique, it differs from a conventional dual-comb spectroscopy scheme, which is intended to measure the spectral response of a sample regardless the temporal properties of the probe signal. In order to generate the trains of optical chirps, we employ a setup that consists of a single bidirectional FSL fed by a narrow linewidth CW laser. This system is implemented with conventional telecommunication components and sinusoidal driving signals with a bandwidth below 100 MHz. The generated optical chirps have a bandwidth approaching 30 GHz and their chirp rates are readily controlled by the frequency signals that drive a couple of AO shifters. This architecture has been demonstrated to allow coherent averaging over times close to one second [36], a scale that turns out to be sufficient to perform the analog pulse compression and the supporting signal processing procedures. As a laser range finder, the system achieves a range resolution of a few millimeters, equivalent to that of time-of-flight pulse lidars with pulses in the range of tens of ps. Moreover, the systems shows a precision of 20 µm with a digitization bandwidth reduced by three orders of magnitudes, from tens of gigahertz to tens of megahertz, as compared to its digital counterpart [16]. Concerning the AR, the other fundamental lidar parameter, it has been shown to be extensible by a factor of ten by concatenation of perfect correlation phase codes. Finally, and unlike incoherent pulse compression approaches, our ranging system inherently provides phase-sensitive measurements. To demonstrate and evaluate this capability, we have retrieved the time-dependent complex response of a sample (a phase modulator driven by an RF signal on the sub-millisecond time scale). Additionally, our ranging system can work as a velocimeter, by measuring the Doppler shift induced on the probe comb. As a final benefit, the temporal waveforms generated by the setup are easily tailorable while preserving its TBP product, and can be set in the form of quasi-continuous waveforms amenable to high-power amplification.

The present approach also opens up prospects for future developments. In order to improve the range resolution, the bandwidth of the dual-comb generator could be increased to values near 100 GHz (>1000 optical lines) by a proper design of the FSL, as has been already demonstrated for a unidirectional loop [37,45]. In that direction, several analyses have been recently published, in order to model the comb generation in an AO-FSL [44,51]. On the other hand, the possibility of expanding the AR, along with the use of highly amplified long optical chirps, makes our system especially suited for long distance ranging.

Funding. Agencia Estatal de Investigación (TEC2017-89688-P); Generalitat Valenciana (PROMETEO/2020/029); Universitat Jaume I (UJI-B2019-45); Association Nationale de la Recherche et de la Technologie; Spanish Government (RTI2018-097957-B-C32); Agence Nationale de la Recherche (ANR 14-CE32-0022, ANR 16-ASTR-015).

Acknowledgments. We thank Dr. Olivier Jacquin and Dr. Olivier Hugon for their help with the Lidar experiments. VD acknowledges financial support from Spanish MICINN under the contract RYC-2017-23668.

Disclosures. The authors declare no conflicts of interest.

Optics EXPRESS

Data availability. Data underlying the results presented in this paper may be obtained from the authors upon reasonable request.

References

1. J. P. von der Weid, R. Passy, G. Mussi, and N. Gisin, "On the characterization of optical fiber network components with optical frequency domain reflectometry," J. Lightwave Technol. **15**(7), 1131–1141 (1997).
2. D. W. Dolfi, M. Nazarathy, and S. A. Newton, "5-mm-resolution optical-frequency-domain reflectometry using a coded phase-reversal modulator," Opt. Lett. **13**(8), 678–680 (1988).
3. M.-C. Amann, T. Bosch, M. Lescure, R. Myllylä, and M. Riox, "Laser ranging: a critical review of usual techniques for distance measurement," Opt. Eng. **40**(1), 10–19 (2001).
4. S. Royo and M. Ballesta-Garcia, "An overview of lidar imaging systems for autonomous vehicles," Appl. Sci. **9**(19), 4093 (2019).
5. D. Tosi, E. Schena, C. Molardi, and S. Korganbayev, "Fiber optic sensors for sub-centimeter spatially resolved measurements: Review and biomedical applications," Opt. Fiber Technol. **43**, 6–19 (2018).
6. D. Uttam and B. Culshaw, "Precision time domain reflectometry in optical fiber systems using a frequency modulated continuous wave ranging technique," J. Lightwave Technol. **3**(5), 971–977 (1985).
7. G. Berkovic and E. Shafir, "Optical methods for distance and displacement measurements," Adv. Opt. Photonics **4**(4), 441–471 (2012).
8. M. U. Piracha, D. Nguyen, D. Mandridis, T. Yilmaz, I. Ozdur, S. Ozharar, and P. J. Delfyett, "Range resolved lidar for long distance ranging with sub-millimeter resolution," Opt. Express **18**(7), 7184–7189 (2010).
9. Y. Li, A. Rashidinejad, J.-M. Wun, D. E. Leaird, J.-W. Shi, and A. M. Weiner, "Photonic generation of W-band arbitrary waveforms with high time-bandwidth products enabling 3.9 mm range resolution," Optica **1**(6), 446–454 (2014).
10. N. Kuse and M. E. Fermann, "Frequency-modulated comb LIDAR," APL Photonics **4**(10), 106105 (2019).
11. R. I. MacDonald, "Frequency domain optical reflectometer," Appl. Opt. **20**(10), 1840–1844 (1981).
12. W. Zou, S. Yang, X. Long, and J. Chen, "Optical pulse compression reflectometry: proposal and proof-of-concept experiment," Opt. Express **23**(1), 512–522 (2015).
13. J. Pan, J. Zhou, X. Yi, Q. Sui, C. Lu, and Z. Li, "Multi-Dimensional optical fiber sensing enabled by digital coherent optical technologies," J. Lightwave Technol. **37**(11), 2488–2501 (2019).
14. A. Bergman, T. Langer, and M. Tur, "High spatial resolution, low-noise Brillouin dynamic gratings reflectometry based on digital pulse compression," Opt. Lett. **41**(15), 3643–3646 (2016).
15. S. Pan and Y. Zhang, "Microwave photonic radars," J. Lightwave Technol. **38**(19), 5450–5484 (2020).
16. J. Clement, C. Schnébelin, H. Guillet de Chatellus, and C. R. Fernández-Pousa, "Laser ranging using coherent pulse compression with frequency shifting loops," Opt. Express **27**(9), 12000–12010 (2019).
17. V. Billault, G. Arpison, V. Crozatier, V. Kemlin, L. Morvan, D. Dolfi, and H. Guillet de Chatellus, "Coherent Optical Fiber Sensing Based on a Frequency Shifting Loop," J. Lightwave Technol. **39**(12), 4118–4123 (2021).
18. J. J. Mompó, L. Shiloh, N. Arbel, N. Levanon, A. Loayssa, and A. Eyal, "Distributed dynamic strain sensing via perfect periodic coherent codes and a polarization diversity receiver," J. Lightwave Technol. **37**(18), 4597–4602 (2019).
19. K. Shemer, G. Bashan, H. Hagai Diamandi, Y. London, T. Raanan, Y. Israelashvili, A. Charny, I. Cohen, A. Bergman, N. Levanon, and A. Zadok, "Sequence-coded coherent laser ranging with high detection sensitivity," OSA Continuum **3**(5), 1274–1282 (2020).
20. D. Kravitz, D. Grodensky, N. Levanon, and A. Zadok, "High-resolution low-sidelobe laser ranging based on incoherent pulse compression," IEEE Photonics Technol. Lett. **24**(23), 2119–2121 (2012).
21. N. Arbel, L. Hirschbrand, S. Weiss, N. Levanon, and A. Zadok, "Continuously operating laser range finder based on incoherent pulse compression: noise analysis and experiment," IEEE Photonics J. **8**(2), 1–11 (2016).
22. S. A. Diddams, "The evolving optical frequency comb," J. Opt. Soc. Am. B **27**(11), B51–B62 (2010).
23. V. Durán, S. Tainta, and V. Torres-Company, "Ultrafast electrooptic dual-comb interferometry," Opt. Express **23**(23), 30557–30569 (2015).
24. I. Coddington, W. C. Swann, L. Nenadovic, and N. R. Newbury, "Rapid and precise absolute distance measurements at long range," Nat. Photonics **3**(6), 351–356 (2009).
25. N. R. Newbury, I. Coddington, and W. Swann, "Sensitivity of coherent dual-comb spectroscopy," Opt. Express **18**(8), 7929–7945 (2010).
26. T.-A. Liu, N. R. Newbury, and I. Coddington, "Sub-micron absolute distance measurements in sub-millisecond times with dual free-running femtosecond Er fiber-lasers," Opt. Express **19**(2), 512–522 (2011).
27. R. Yang, F. Pollinger, K. Meiners-Hagen, J. Tan, and H. Bosse, "Heterodyne multi-wavelength absolute interferometry based on a cavity-enhanced electro-optic frequency comb pair," Opt. Lett. **39**(20), 5834–5837 (2014).
28. E. L. Teleanu, V. Durán, and V. Torres-Company, "Electro-optic dual-comb interferometer for high-speed vibrometry," Opt. Express **25**(14), 16427–16436 (2017).
29. H. Wu, T. Zhao, Z. Wang, K. Zhang, B. Xue, J. Li, M. He, and X. Qu, "Long distance measurement up to 1.2 km by electro-optic dual-comb interferometry," Appl. Phys. Lett. **111**(25), 251901 (2017).

Optics EXPRESS

30. P. Trocha, M. Karpov, D. Ganin, M. H. P. Pfeiffer, A. Kordts, S. Wolf, J. Krockenberger, P. Marin-Palomo, C. Weimann, S. Randel, W. Freude, T. J. Kippenberg, and C. Koos, "Ultrafast optical ranging using microresonator soliton frequency combs," Science **359**(6378), 887–891 (2018).
31. M. G. Suh and K. J. Vahala, "Soliton microcomb range measurement," Science **359**(6378), 884–887 (2018).
32. J. Riemensberger, J. Riemensberger, A. Lukashchuk, M. Karpov, W. Weng, E. Lucas, J. Liu, and T. J. Kippenberg, "Massively parallel coherent laser ranging using a soliton microcomb," Nature **581**(7807), 164–170 (2020).
33. I. Coddington, N. Newbury, and W. Swann, "Dual-comb spectroscopy," Optica **3**(4), 414–426 (2016).
34. Z. Zhu and G. Wu, "Dual-comb ranging," Engineering **4**(6), 772–778 (2018).
35. S. A. Van den Berg, S. T. Persijn, G. J. P. Kok, M. G. Zeitouny, and N. Bhattacharya, "Many-wavelength interferometry with thousands of lasers for absolute distance measurement," Phys. Rev. Lett. **108**(18), 183901 (2012).
36. V. Duran, L. Djevarhidjian, and H. Guillet de Chatellus, "Bidirectional frequency-shifting loop for dual-comb spectroscopy," Opt. Lett. **44**(15), 3789–3792 (2019).
37. H. Guillet de Chatellus, L. Romero Cortés, C. Schnébelin, M. Burla, and J. Azaña, "Reconfigurable photonic generation of broadband chirped waveforms using a single CW laser and low-frequency electronics," Nat. Commun. **9**(1), 2438 (2018).
38. Z. Zhang, Y. Liu, M. Burla, and B. J. Eggleton, "5.6-GHz-bandwidth photonic stepped-frequency radar using MHz-level frequency-shifting modulation," *2020 Conference on Lasers and Electro-Optics (CLEO)*, 2020, pp. 1–2.
39. X. Ren, B. Xu, Q. Fei, Y. Liang, J. Ge, X. Wang, K. Huang, M. Yan, and H. Zeng, "Single-photon counting laser ranging with optical frequency combs," IEEE Photonics Technol. Lett. **33**(1), 27–30 (2021).
40. P. Coppin and T. G. Hodgkinson, "Novel optical frequency comb synthesis using optical feedback," Electron. Lett. **26**(1), 28–30 (1990).
41. H. Guillet de Chatellus, E. Lacot, W. Glastre, O. Jacquin, and O. Hugon, "Theory of Talbot lasers," Phys. Rev. A **88**(3), 033828 (2013).
42. H. Guillet de Chatellus, O. Jacquin, O. Hugon, W. Glastre, E. Lacot, and J. Marklof, "Generation of ultrahigh and tunable repetition rates in CW injection-seeded frequency-shifted feedback lasers," Opt. Express **21**(13), 15065–15074 (2013).
43. V. Durán, H. Guillet de Chatellus, C. Schnebélin, K. Nithyanandan, L. Djevarhidjian, J. Clement, and C. R. Fernández-Pousa, "Optical frequency combs generated by acousto-optic frequency-shifting loops," IEEE Photonics Technol. Lett. **31**(23), 1878–1881 (2019).
44. N. Kanagaraj, L. Djevarhidjian, V. Duran, C. Schnebelin, and H. Guillet de Chatellus, "Optimization of acousto-optic optical frequency combs," Opt. Express **27**(10), 14842–14852 (2019).
45. H. Guillet de Chatellus, L. Romero Cortés, and J. Azaña, "Arbitrary energy-preserving control of the line spacing of an optical frequency comb over six orders of magnitude through self-imaging," Opt. Express **26**(16), 21069–21085 (2018).
46. C. Schnébelin and H. Guillet de Chatellus, "Agile photonic fractional Fourier transformation of optical and RF signals," Optica **4**(8), 907–910 (2017).
47. C. Schnébelin, J. Azaña, and H. Guillet de Chatellus, "Programmable broadband optical field spectral shaping with megahertz resolution using a simple frequency shifting loop," Nat. Commun. **10**(1), 4654 (2019).
48. J. Clement, H. Guillet de Chatellus, and C. R. Fernández-Pousa, "Far-field Talbot waveforms generated by acousto-optic frequency shifting loops," Opt. Express **28**(9), 12977–12997 (2020).
49. E. Rubiola, *Phase Noise and Frequency Stability in Oscillators*, (Cambridge University, 2008).
50. L. Levanon and E. Mozeson, *Radar Signals*, (Wiley, 2004).
51. S. N. Mantsevich, M. I. Kupreychik, and V. I. Balakshy, "Possibilities of wide-angle tellurium dioxide acousto-optic cell application for the optical frequency comb generation," Opt. Express **28**(9), 13243–13259 (2020).